Thin Film BCZT in a Capacitive Thermo-Electric Converter

By

Emily Thomson

Submitted to the
Department of Materials Science and Engineering
In Partial Fulfillment of the Requirements for the Degree of
Bachelor of Science in Materials Science and Engineering

At the

Massachusetts Institute of Technology

June 2016

Signature of Author: _____

Department of Materials Science and Engineering

June 2016

Certified by: _____

Yang Shao-Horn
W.M. Keck Professor of Energy
Thesis Supervisor

Accepted by: _____

Geoffrey S.D. Beach
Class of '58 Associate Professor of Materials Science and Engineering
Undergraduate Committee Chair

Table of Contents

Thin Film BCZT in a Capacitive Thermo-Electric Converter

By

Emily Thomson

Submitted to the
Department of Materials Science and Engineering
On May 3 2016 in Partial Fulfillment of the Requirements for the Degree of
Bachelor of Science in Materials Science and Engineering

Abstract

Thin film BCZT was processed, optimized, and analyzed from powder to ceramic to film for use in a capacitive thermos-electric converter. The idea of using a temperature dependent dielectric to turn heat into electricity has been around for several decades but has never been feasible due to low efficiency and the practical difficulty of being able to thermally cycle the dielectric material quickly enough. However, thin film materials are able to be thermally cycled at high enough frequencies. One material that has potential to be used as the dielectric in a capacitive thermo-electric converter is $Ba(Ti_xZr_{1-x})O_3$-$(Ba_yCa_{1-y})TiO_3$. Known as BCZT, this perovskite has previously been studied as an alternative to piezoelectrics which are traditionally made with lead. BCZT has a very high dielectric constant of several thousand and, because of its triple point just above room temperature, the dielectric constant is temperature dependent around room temperature. In this paper, BCZT is studied for its potential as a thin film dielectric material in a capacitive thermo-electric converter. Several different compositions around the triple point are created from powder sources, sintered into targets for PLD, analyzed, and the most promising composition was deposited into a thin film and patterned with in-plane capacitor contacts. Analysis using XRD and dielectric measurements was done at several stages.

Thesis Supervisor: Yang Shao-Horn

Title: W.M. Keck Professor of Energy

Introduction

Research in the areas of energy conversion and storage is of crucial importance for increasing the efficiency and sustainability of modern devices and technologies. One potential advancement in this area is developing a thermo-electric converter. A thermo-electric converter is a device which converts excess heat, such as the heat given off by batteries in phones and laptops, into electricity. Though this is has been achieved in the past using the Seebeck effect and pyroelectric effect, another method which has shown promise is to use a capacitor with a dielectric material whose permittivity changes with temperature.

The capacitive thermo-electric converter has several advantages over a device which makes use of the Seebeck or pyroelectric effect such as higher efficiency and more compactness. An effective, cost effective, lead-free capacitive thermo-electric converter would fill a gap in technology. Prior research has shown that this idea is plausible, but several issues have been highlighted which have deterred this idea from being pursued. Using a thin film capacitive structure and a promising material, BCZT, it is hopeful that a capacitive thermo-electric converter could become practical for some applications.

Background

There are several similar methods for turning heat into electricity using other materials properties such as the Seebeck effect and the pyroelectric effect. The pyroelectric effect is exhibited in the materials in the ten polar crystal classes. When polar materials are heated, the dipole moment decreases, leading to a current flow across the material. By cycling the material between hot and cold temperatures, an alternating current is generated. Pyroelectric materials were first proposed as thermo-electric converters in the 1950's and several iterations since then have made improvements. However, this method of turning heat into electricity has limited potential because of a low theoretical conversion efficiency and limited operating frequency. [12] Thermo-electric converters using pyroelectricity reaches efficiency of about .03-.06%, assuming a 10-20 K temperature difference[3].

A more common method of converting heat into electricity is making use of the Seebeck effect. When two dissimilar conductive materials are in contact with each other, a temperature gradient across the materials will result in a voltage across the interface due to the gradient in concentration of charge carriers. While this effect is commonly used in thermocouples to measure temperature, it can also be used to generate electricity from heat. Even with recent advances in this type of thermo-electric converter such as nanoscaling, it remains too inefficient and costly to be practical.[4,5]

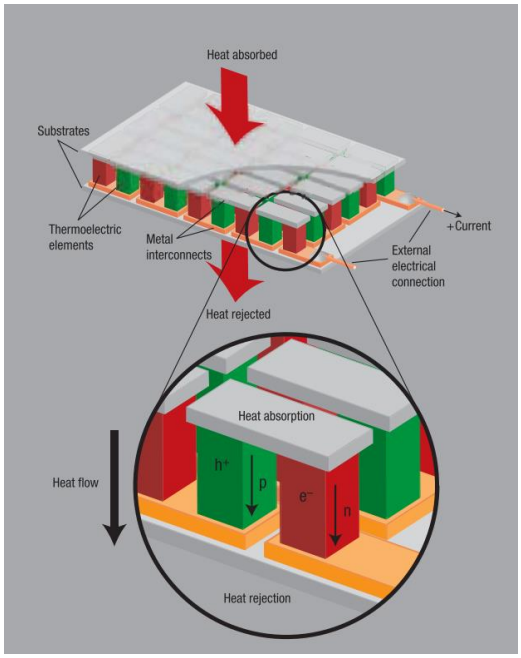

Figure 1: Schematic of a device which uses a temperature gradient to create a voltage. To make thermoelectric converters using the Seebeck effect, many material junctions are used in series to generate a significant voltage.[4]

Though a there is demand for a technology that would convert wasted heat into electricity to improve the energy efficiency of devices and processes, neither pyroelectric nor Seebeck effect thermo-electric converters have proven to be very efficient and are not cost effective for widespread applications. Another proposed method of thermo-electric conversion is to use a capacitor with a dielectric material whose permittivity changes with temperature.

The principle of operation of a capacitive thermo-electric converter is as follows. The device would work using a capacitor with a special dielectric material whose dielectric constant changes with temperature around the operating temperature. It relies on the fact that capacitance is proportional to the dielectric constant according to the equation $C = \varepsilon * A/d$. As the dielectric constant increases, the amount of charge stored on the capacitor also increases. By cycling the temperature and voltage on the capacitor appropriately (as described below), electricity can be generated.

There were several papers published in the 1960's on the feasibility of creating capacitive thermo-electric converters. Clingman and Moore[6] estimate the theoretical efficiency for this type of thermo-electric converter. In their calculations, they make several assumptions about the device design. A temperature difference of around 30℃ is used in these calculations. The calculations were done for a barium titanate dielectric with a Curie-Weiss constant of 1.7×10^5 K. They describe a heating a charging cycle shown in Figure 2:

1) The capacitor is not charged, and at room temperature (T1).
2) The capacitor is charged (Q1), and at room temperature (T1).
3) The capacitor is kept at constant charge (Q1), and heated (T2), causing an increase in voltage.
4) It is kept at T2 and the charge is released into the rechargeable battery.
5) The neutral capacitor is brought back to T1.

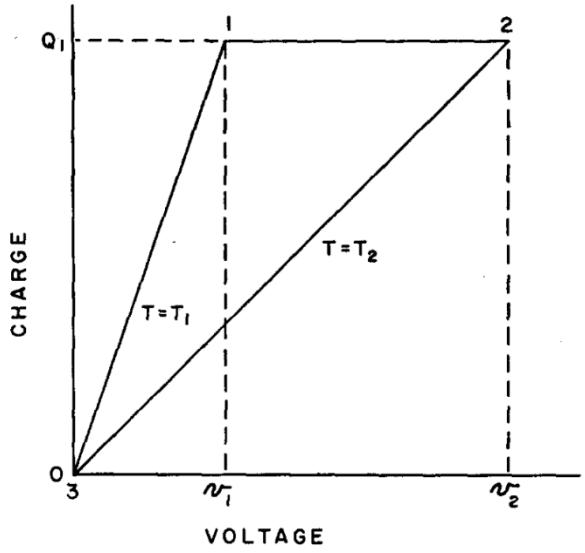

Figure 2: Diagram shows the cycle of temperature and voltage used to generate electricity from heat. [6]

Using this cycle, an efficiency of 1-3% is calculated. For comparison, the Carnot efficiency of a heat engine at this temperature is around 7%. Despite this low efficiency, Clingman and Moore suggest that this type of thermo-electric converter may have applications where a lightweight device is needed and where both a hot and cold source are present for thermal cycling.

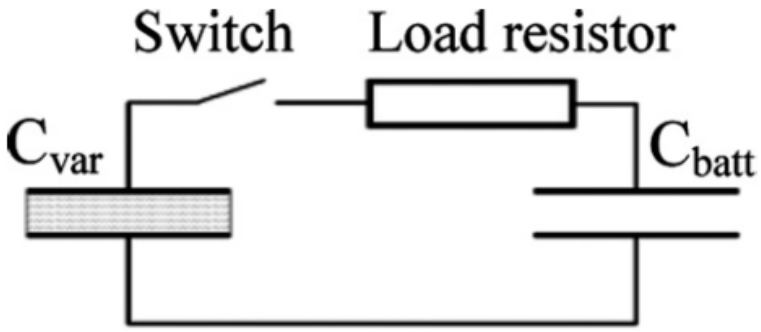

Figure 3: Schematic of a simple circuit that would allow the thermal and voltage cycling to be achieved. It contains a capacitor with variable dielectric, a rechargeable battery, and a switch to open and close the circuit. [3]

Childress also estimated the theoretical efficiency of a capacitive thermo-electric converter using a barium titanate dielectric material.[7] He calculated a theoretical maximum efficiency of approximately .5%. In this estimation, the same temperature difference as Clingman and Moore and the same type of thermal and electrical cycling for the generation of electricity were used. He approximated a more accurate permittivity behavior for polycrystalline ferroelectrics. Additionally, he estimated the power output of a $BaTiO_3$ thermo-electric converter as 900 Watts per kilogram. While these efficiency and power output estimations were calculated using an ideal hysteresis loop, Childress asserts that it is a very close approximation to reality.

Both of these early theoretical studies of capacitive thermo-electric converters have suggested practical difficulties of thermally cycling a material quickly enough for the device to be effective. However, by making the device using a thin film, it should be possible to cycle between hot and cold temperatures quickly. Because the material is so thin, heat transfer is very

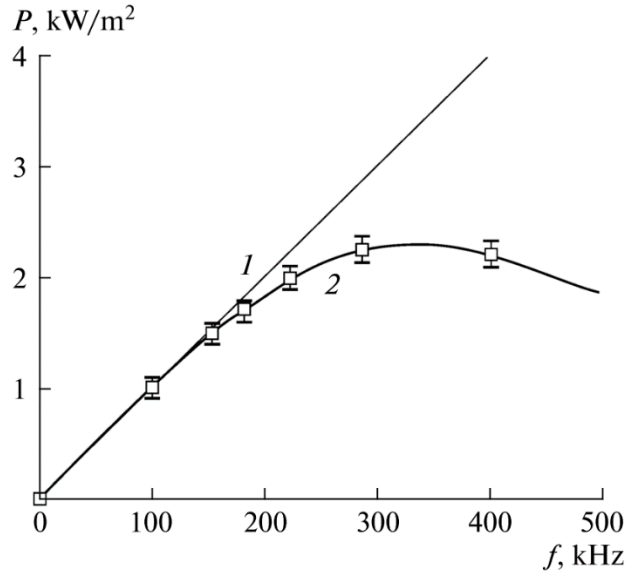

Figure 4: Calculated power output at different frequencies of thermal cycling for a $Ba_{0.3}Sr_{0.7}TiO_3$ film[8]

rapid. Early assessments of this converter did not consider using thin films; for instance Childress assumed a thickness of .1 mm in his paper. Additionally, the use of BCZT as the dielectric has not been studied previously and has several promising properties such as a high capacitance which increases the power output of the device.[8]

Another study was done in 2012 to estimate the power output of a barium strontium titanate thin film thermo-electric converter.[8] It was estimated that the power output by a 1 micrometer thick thermo-electric converter could be as high as 2.3 kW/m^2 if a 300 kHz cycling frequency is achieveable. However, it was estimated that a 1 micrometer thick barium strontium titanate film can be cycled between hot and cold in a period of 10 microseconds, which corresponds to a frequency of 100 kHz. This paper states that the main factors limiting power

production are capacitance, frequency of the heating and cooling cycle, and working temperature

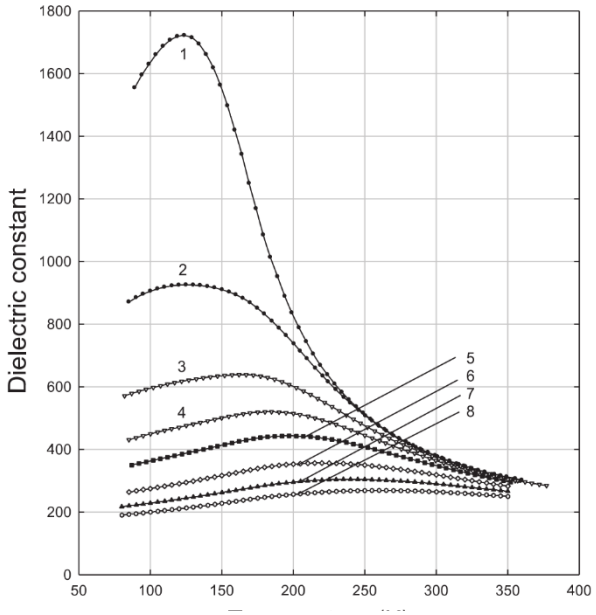

Figure 5: Dielectric field changes with temperature found experimentally for barium strontium titanate thin film. Electric field increases from 0 V/μm (curve 1) to 60 V/μm (curve 8)[3]

range.

A thin film capacitive thermo-electric converter was fabricated and studied as a proof of concept.[3] It was made using a .5 micrometer thick $Ba_{0.3}Sr_{0.7}TiO_3$ film. This material was chosen because it could have a short thermal cycle time and high power output per cycle. Figure 5 shows that dielectric constant changes significantly with temperature, which is the key property to making this device function. The device was operated between 280-310 K and high frequency thermal cycling of 100 kHz was achieved using MEMS. They were able to obtain an effeciency of .4% which is close to the theoretically predicted efficiency.

BCZT (barium calcium zirconium titanate) is a material that has a perovskite structure. In previous work, this material had proven promising as being a dielectric with a permittivity that changes with temperature. BCZT has been studied as an alternative to typical piezoelectrics

which contain lead. High permittivity and sharp temperature dependence near the phase transition make it appealing for an application as the dielectric in a capacitive thermo-electric converter. Its triple point around room temperature is what gives it these properties. The triple point has been experimentally determined to be at 32% BZT at a temperature of 57℃ as Figure 6, the phase diagram of BZT-BCT, shows. [9]

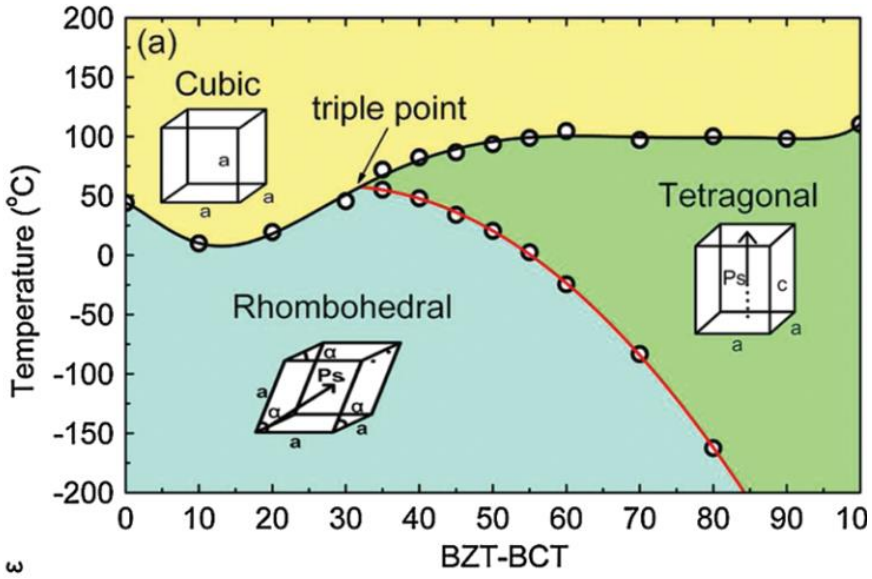

Figure 6: Phase diagram of BZT-BCT shows the triple point at 57 ℃. [9]

This phase diagram uses the notation $x\mathrm{Ba}(\mathrm{Ti}_{.8}\mathrm{Zr}_{.2})\mathrm{O}_3$-$y(\mathrm{Ba}_{.7}\mathrm{Ca}_{.3})\mathrm{TiO}_3$, shortened to BZT – BCT. Unfortunately, various papers on this subject use different naming schemes which makes it difficult to directly compare the work done by each. For instance, Fang et al describe BCZT as being a pseudoternary system, meaning that it is composed of three species ($x\mathrm{BaTiO}_3$-$y\mathrm{CaTiO}_3$-$z\mathrm{BaZrO}_3$). The abbreviation used in this report, *x*CT-*y*BZ, denotes the amount of calcium in the barium lattice sites (x) and the amount of zirconium in the titanium sites (y).

Perovskite is a class of dielectric materials of the composition ABO_3. The A and B sites are both negatively charged ions where the A and B sites are typically of significantly sizes. In

BCZT, the A sites are primarily barium with doped calcium and the B sites are primarily titanium with doped zirconium. Figure 7 shows the cubic form of a perovskite which is the equilibrium phase above the Curie point.

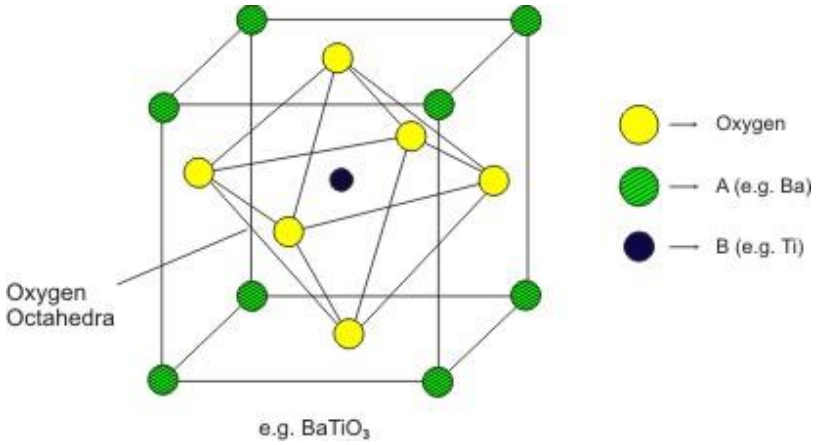

Figure 7: Unit cell of a perovskite material has structure ABO_3. BCZT has Ba and Ca on the A sites and Ti and Zr on the B sites. *(http://nptel.ac.in/courses/113104005/lecture4/4_2.htm)*

Another consideration concerning the phases of BCZT is the existence of the pyrochlore phase impurity which Fang et al discuss in their paper. They found that they pyrochlore phase can be identified in XRD by a peak around $2\theta = 30$, just before the {110} peak as shown in

Figure 8. [10] Pyrochlore is a phase similar to the perovskite but with composition $A_2B_2O_6$ and $A_2B_2O_7$.

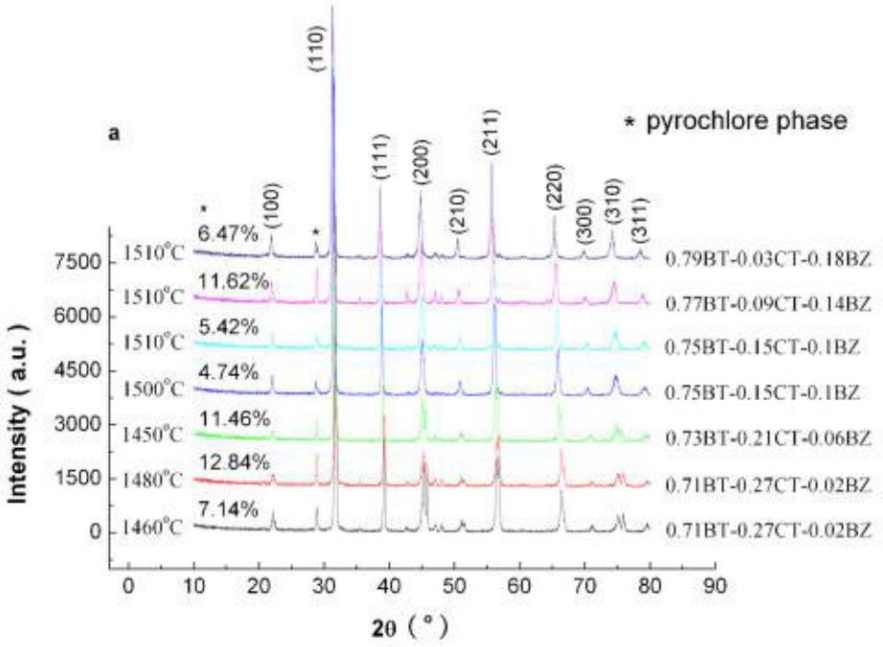

Figure 8: XRD pattern identifyinng the location of the pyrochlore phase in BCZT at $2\theta = 30$. [10]

The XRD peaks of the crystallographic planes of BCZT have been studied, but are not in the database of High Score Plus. In this paper, peaks were identified by comparing XRD patterns to previous work. In particular, Liu and Ren measured in-situ XRD was taken during cooling to show the difference in XRD pattern between the tetragonal and rhombohedral phases. [9] Their results, shown in Figure 9, show a shift between a single peak and double peak from the rhombohedral phase to tetragonal phase.

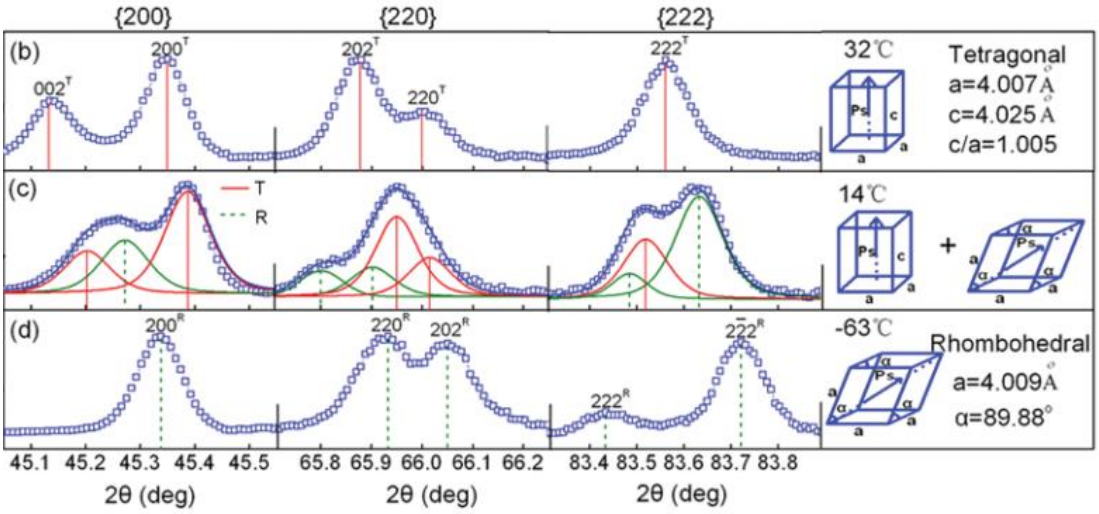

Figure 9: XRD of BCZ in the tetragonal, rhombohedral, and transition phases

The technique used to create the thin films of BCZT is pulsed laser deposition (PLD). PLD is a good technique for growing films using a variety of materials onto almost any substrate. It is better suited for oxide materials than other thin film deposition methods such as sputtering or thermal evaporation which require a conductive material and a material with a relatively low melting point respectively. A high powered laser (10^{12}-10^{15} W/cm^2) is pointed at a bulk target of the desired material. This knocks off micron-sized bits of material which then form a plume. The plume can be controlled by varying the laser power, pressure in the chamber, and distance between the substrate and the target. When the plume hits the substrate, particles stick and, due to the high temperature, are able to rearrange to an equilibrium crystal which is epitaxial if there is a close lattice match. A schematic of this process is shown in Figure 10.

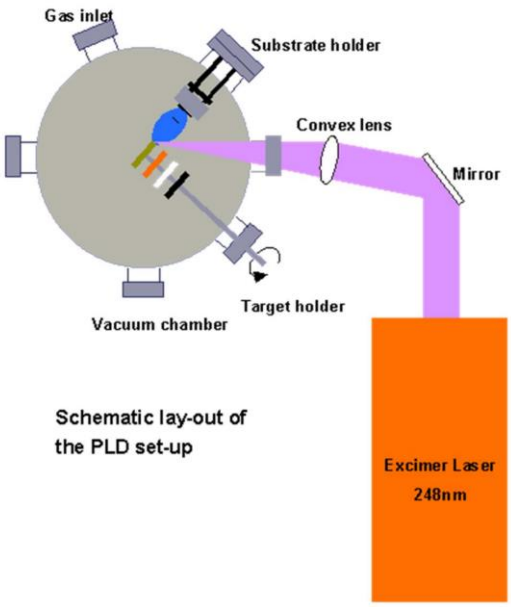

Figure 10: Schematic of a PLD setup shows the laser, target, plume, and substrate. [11]

Experimental Procedures

There were five main processing steps in the fabrication of this device, with analysis between every step:

Powder => Puck => Target => Film => Device

Six compositions of BCZT powder were made around the composition that contains the triple point. The sources of Barium, Calcium, Zirconium, and Titanium were Barium carbonate (BaCO3 99.997%, AlfaAesar), calcium carbonate (CaCO3 99.95%, AlfaAesar), zirconium dioxide (ZrO2 99.978%, AlfaAesar) and titanium oxide (TiO2 99.995%, LTS Research Laboratories Inc). The chemical reaction that takes place is here[10]:

$$(1-y)\mathrm{BaCO_3}+y\mathrm{CaCO_3}+(x+y)\mathrm{TiO_2}+(1-x-y)\mathrm{ZrO_2}\rightarrow\ x\mathrm{BaTiO_3}-y\mathrm{CaTiO_3}-(1-x-y)\mathrm{BaZrO_3}+\mathrm{CO_2}\uparrow$$

The eight powders were made using standard methods, following the technique used by Fang et al[10]. After calculating the needed mass of each source chemical to create the correct stoichiometry, each powder was carefully weighed and then mixed together in a clean crucible. The powders were then calcinated at 1000℃ for 10 hours to decompose carbonates. Next, they were alternately ball milled for 3 hours in acetone and calcinated at 1350℃ for 4 hours a total of five times. XRD was done on the powders by carefully flattening the powder into the sample holder. The eight compositions used, along with abbreviations used in this report, are summarized in this table:

Group A	
Composition	Abbreviation
$(Ba_{0.97}Ca_{0.03})[Ti_{0.82}Zr_{0.18}]O_3$	0.03CT-0.18BZ
$(Ba_{0.91}Ca_{0.09})[Ti_{0.86}Zr_{0.14}]O_3$	0.09CT-0.14BZ
$(Ba_{0.79}Ca_{0.21})[Ti_{0.94}Zr_{0.06}]O_3$	0.21CT-0.06BZ
$(Ba_{0.73}Ca_{0.27})[Ti_{0.98}Zr_{0.02}]O_3$	0.27CT-0.02BZ

Group B	
Composition	Abbreviation
$(Ba_{0.85}Ca_{0.15})[Ti_{1.00}Zr_{0.00}]O_3$	0.15CT-0.00BZ
$(Ba_{0.85}Ca_{0.15})[Ti_{0.92}Zr_{0.08}]O_3$	0.15CT-0.08BZ
$(Ba_{0.85}Ca_{0.15})[Ti_{0.90}Zr_{0.10}]O_3$	0.15CT-0.10BZ
$(Ba_{0.85}Ca_{0.15})[Ti_{0.87}Zr_{0.13}]O_3$	0.15CT-0.13BZ

These six compositions of powders were then pressed into small pucks and sintered. .07 g of powder was measured and then pressed using a die with a diameter of 5 mm using 1 ton of force maintained for 1 minute. The pressed puck was carefully placed into a crucible and sintered. Sintering time and temperature were varied around 1400℃ for 3 hours to find the optimal conditions to create a dense ceramic. 1400℃ was found to be the upper limit of sintering temperature for BCZT because the material begins to melt and stick to the crucible at higher temperatures and Fang et al found that the undesirable pyrochlore phase was very prominent above this temperature.

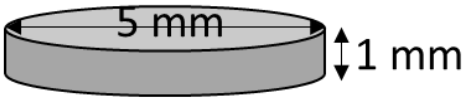

Figure 11: Dimensions of the green puck of pressed BCZT powder.

It is necessary that the ceramic be over 80% dense for PLD, so the sintering process was optimized until this was achieved. The percent density of the ceramic was measured by weighing the ceramic before and after being immersed in water. There was some error in the density measurements. Density was measured by filling pores with water and then measuring the difference in weight of the ceramic with and without water. Though the targets and pucks were boiled in water for 10 minutes, it is possible that the pores were not completely filled with water.

XRD was done on all eight pucks using a Bruker XRD machine. Finally, capacitance vs. temperature measurements were taken as an indicator of the best functioning composition. The most promising composition was then pressed and sintered into a larger disk with a diameter of 25 millimeters and a thickness of approximately 6 mm. The pressure used to press the powder into a green ceramic was increased for the larger target but could not be increased enough to have the same force per unit area do to limitations of the press. Pressure used was increased from 1 ton/19.6mm^2 = .05tons/mm^2 (4.45*10^8 Pa) to 5 tons/490mm^2 = .01 tons/mm^2 (8.9*10^7 Pa).

The capacitance measurements were taken using a low-temperature vacuum measurement system.

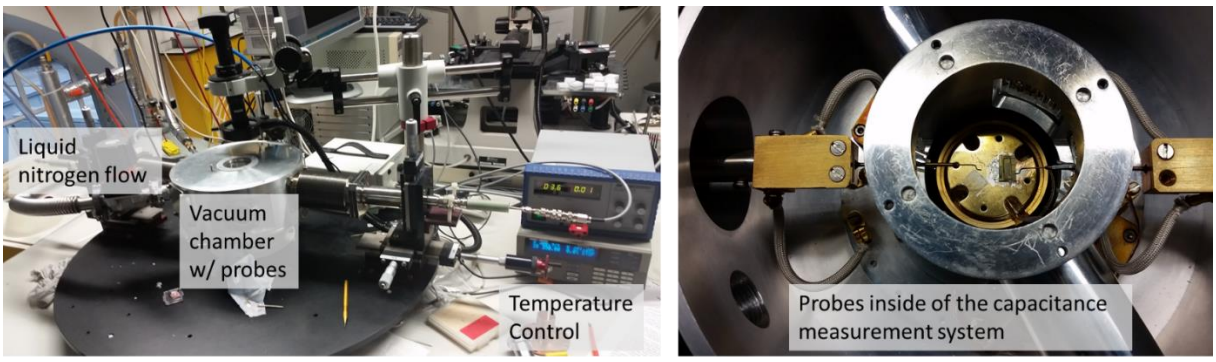

Figure 12: Images of the low temperature capacitance measurement system.

Thin films of BCZT were deposited onto substrates using pulsed laser deposition. An excimer Lambda Physik COPMex laser of wavelength 248 nm and 6 W of power was pulsed at 25 ns. Before depositing, the substrate holder and chamber were wiped clean to reduce contamination. The recipe used was varied around the following recipe (discussed in discussion):

- Pump down pressure of chamber to $3*10^{-5}$ Torr
- Heat substrate to 700℃

- Pump oxygen into chamber to a pressure of 57 mTorr
- Deposit Film for 3000 pulses
- Keep at 550 Torr PO_2 and 700℃ for 20 minutes, then cool down to 200℃ and vent to air.

The thickness of the films were measured using a DEKTAK profilometer. A dot of silver paste was applied to the corner of the substrate before deposition and then removed after deposition so that the thickness could be measured. XRD was done on the films to determine the crystal structure of the films.

Next, the films were patterned with in-plane capacitor contacts using sputtering and photolithography. After the film was cleaned, 5 nm of titanium and then 20 nm of silver were deposited on the film using a Mantis sputtering system. To pattern the silver coating into capacitors, films were coated in photoresist by spin coating at 5000 rotations per minute for 30 seconds. The photoresist was hardened on a 80℃ hot plate for 5 minutes. A mask with a layer of chrome was carefully aligned onto the film and the film was exposed to UV radiation for 35 seconds. After a post-exposure baking at 90℃ for 90 seconds, it was then placed in developer for 20 seconds and washed with deionized water. The pattern was checked under an optical microscope for feature size and finally hard baked at 120 ℃ for 5 minutes.

Next, ion milling was used to remove the metal layer around the patterned photoresist. The samples were placed in the ion milling chamber and milled with accelerated argon ions. Since the layer of photoresist was very thick, the undesired metal layer was removed while the area under the capacitor pattern remained intact. Photoresist was then dissolved using acetone.

Finally, temperature vs. capacitance measurements were done on the in-plane capacitors using two top probes.

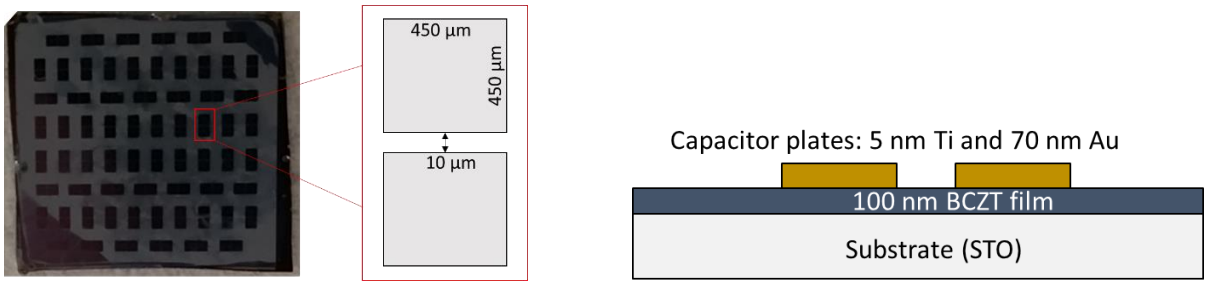

Figure 13: Top (left) and side (right) view of the in-plane capacitor device.

Results and Discussion

The eight sintered pucks of slightly different compositions of BCZT analyzed for crystal structure and electrical properties. From the SEM images of each puck shown in Figure 14, magnified x1300, it can be seen that all of the pucks have a variety of particle sizes.

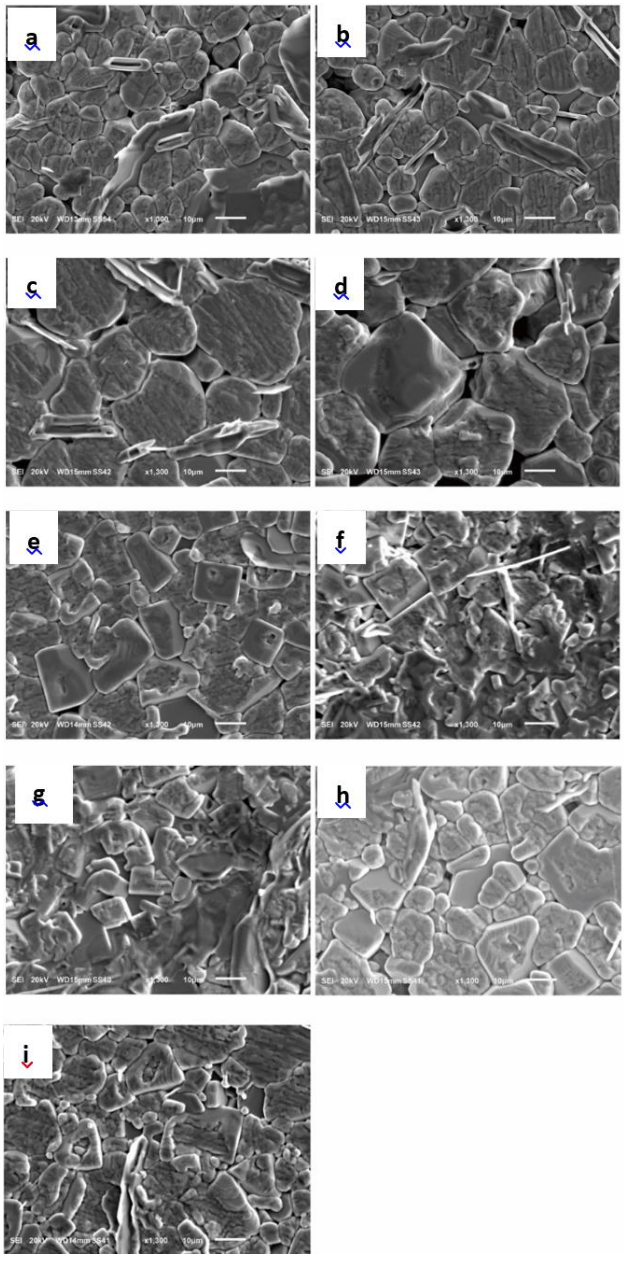

Figure 14: SEM images of (a) 0.15CT-0.13BZ sintered at 1400°C for 3 hours (b) 0.15CT-0.13BZ (c) 0.03CT-0.18BZ (d) 0.09CT-0.14BZ (e) 0.15CT-0.10BZ (f) 0.21CT-0.06BZ (g) 0.27CT-0.02BZ (h) 0.15CT-0.00BZ and (i) 0.15CT-0.08BZ all sintered at 1420°C for 5 hours. Images taken by Zeng Chen (Imperial College MS), used with permission.

Density measurements were also taken of all of the pucks to ensure that the targets would be at least 80% dense, which is necessary for reliable PLD. Density measurements are calculated as a percent of the theoretical density of the single crystal material. The density measurements summarized in Table 1 show that the pucks are adequately dense to be used for PLD.

Table 1: Measured densities of the eight sintered pucks, as a percent of theoretical single crystal density

Composition	Percent Density
.15CT-.00BZ	99.9%
.15CT-.08BZ	96.0%
.15CT-.10BZ	90.9%
.15CT-.13BZ	93.4%
.03CT-.18BZ	90.8%
.09CT-.14BZ	92.9%
.21CT-.06BZ	96.7%
.27CT-.02BZ	96.9%

Capacitance measurements were taken as a function of temperature to assess which composition has the most potential as a thermo-electric conversion device. As is shown in Figure 15, they were taken at four different frequencies. Spreading of the four curves between the frequencies indicates loss in the dielectric, which is not desirable for this application. The phase transitions from rhombohedral to tetragonal and finally to cubic can also be seen as bumps in the curve. Ideally, when the composition is at the triple point, there will only be one bump as the system transitions from rhombohedral to tetragonal. As these plots demonstrate, each phase transition leads to a spike in permittivity so at the triple point the permittivity spikes the most.

By measuring the dimensions of the pucks, it is possible to calculate the permittivity of the bulk BCZT materials using the formula:

$$C = \varepsilon * A/d$$

The overlay plot of Figure 15 shows that the eight compositions display different capacitance behavior over temperature. Some show sharper peaks while others show more broad peaks. If a larger operating temperature range is desired, a broader peak should be used while if more efficiency is needed a composition with a higher change in capacitance over temperature should be chosen.

To use this material as a dielectric in a capacitive thermo-electric converter, it should be in the cubic paraelectric phase. Both the tetragonal and rhombohedral phases are ferroelectric which is problematic because of the hysteresis loop. The best composition therefore has the steepest slope in the cubic region (which corresponds to being at the triple point) and the least spread between the curves of the four frequencies. The two compositions with the most spread are .15CT-.10BZ, .15CT-.08BZ, and .03CT-.18BZ. In order to determine which composition has the most change in dielectric, the derivatives of these plots are shown in Figure 16. The two compositions with the highest change in permittivity that don't have significant spread are 03CT-.18BZ and .27CT-.02BZ.

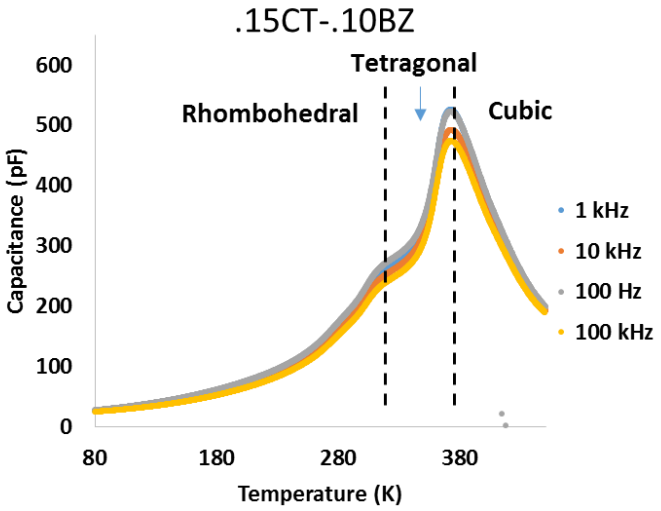

Figure 15:Low temperature capacitance measurement on a sintered BCZT puck at four different frequencies. The temperatures at which the two phase transitions happen can be identified by the change in slope.

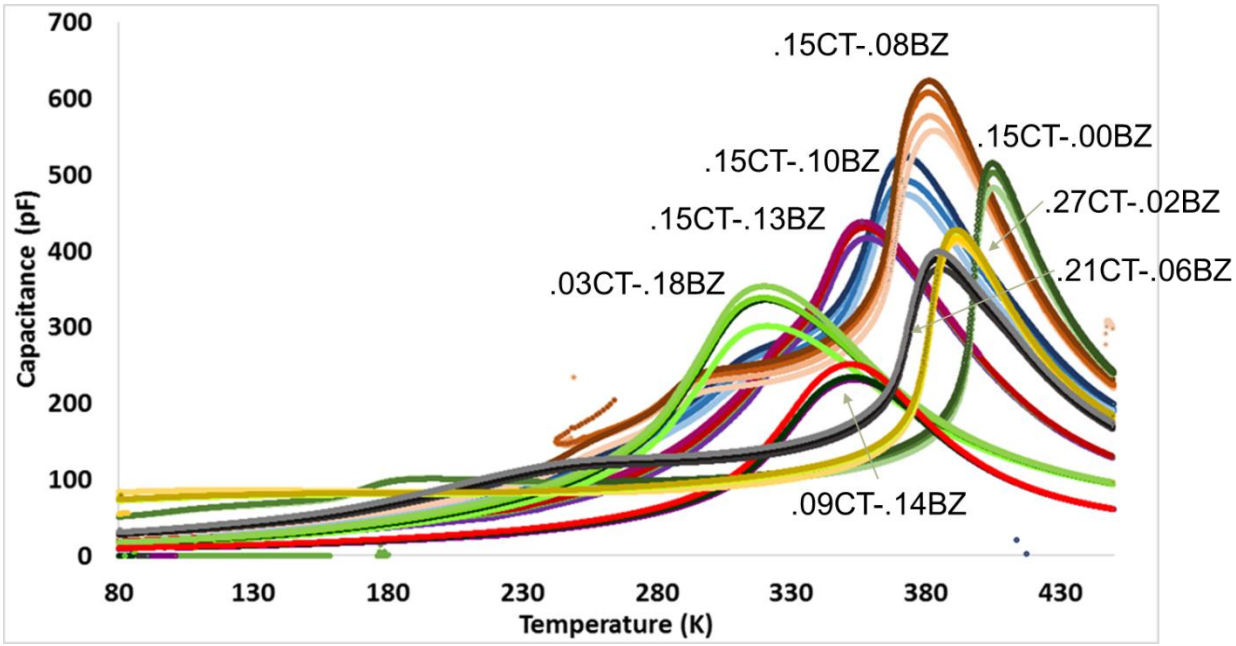

Figure 16: Overlay of the capacitance measurements from all 8 compositions taken from 78 K-450 K shows the variety of dielectric behavior that can be achieved by varying composition.

XRD plots, shown in Figure 17, were taken of all eight pucks. As expected, the peaks generally match up with peaks measured in previous research[12]. Of note in these XRD plots are small shifts in peak location, peaks that split into two peaks, and the existence of the secondary pyrochlore phase as discussed in the background section. XRD was done at room temperature (around 25℃), so according to the phase diagram the material should be primarily in the rhombohedral phase especially with low concentrations of calcium. As the concentration of calcium increases and the composition shifts right on the phase diagram, the material is expected to shift into the rhombohedral phase.

Comparing these XRD plots with the XRD plots from previous work shown in Figure 9 allow these compositions to be identified as rhombohedral or tetragonal. In the top four plots, calcium doping in barium is held constant while zirconium doping in titanium sites is increased from pure titanium to $Ti_{.87}Zr_{.13}$. In the bottom four curves, the calcium doping in barium is increasing from top to bottom while the zirconium doping in titanium is decreasing from top to bottom.

Figure 9 shows the {200} peak at 45.4 as a single peak for rhombohedral structure but a double peak at 45.1 2θ and 45.4 2θ for tetragonal structure. From the XRD plots in Figure 18, which shows the {200} peak taken with a higher quality XRD machine for better resolution, it appears that .15CT-0BZ, .21CT-.06BZ, and .27CT-.02BZ all show distinct double {200} peaks and are therefore tetragonal. The .03CT-.18BZ and .15CT-.13BZ compositions show single peaks, indicating a rhombohedral phase. The other three compositions show one stronger peak with some amount of an indistinct second peak. This indicates that there the composition is near the phase transition between rhombohedral and tetragonal and that there is a mixture of both phases in the material.

Peak shifting towards higher 2θ means that the d-spacing of that plane has decreased. Since zirconium is a larger molecule than titanium and barium is a larger molecule than calcium, it is predicted that an increase in zirconium and barium concentrations would lead to peaks at higher 2θ. The XRD peaks in Figure 17 support this. The top four curves show increasing zirconium content while calcium content stays the same, and the peaks shift slightly to higher 2θ as the zirconium content increases.

The existence of the pyrochlore phase, which is not a desirable phase for this application, can be identified by a small peak at around $2\theta = 30$. Figure 17 shows small amounts of this phase in all compositions. The differences between the pyrochlore peaks are too small to reasonably show trends. However, prior research suggests that higher sintering temperature and calcium concentration leads to a larger pyrochlore phase.

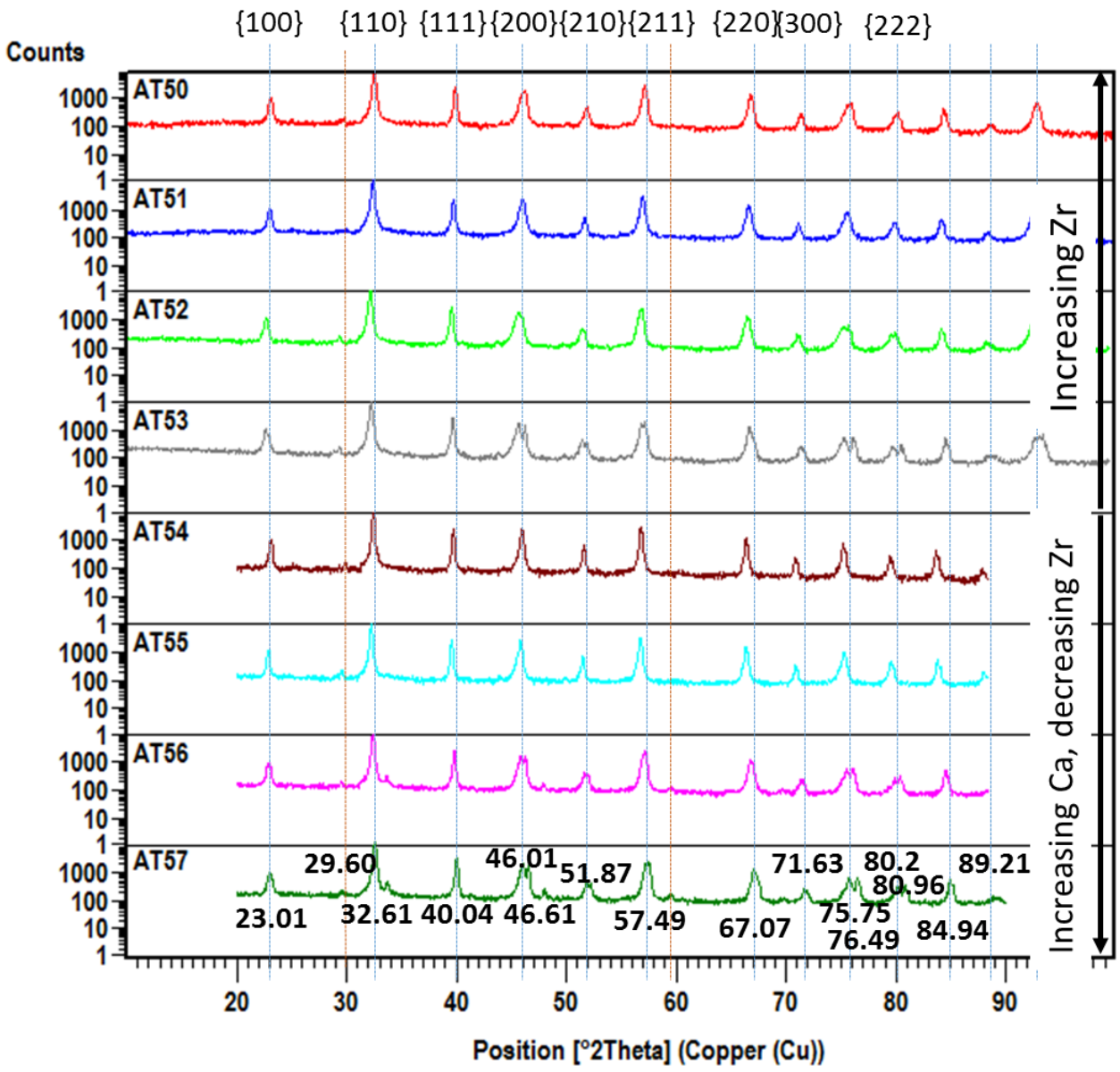

Figure 17: XRD patterns of each composition showing small differences in crystal structure. Compositions from top to bottom: .15CT-.10BZ, .15CT-.13BZ, .15CT-.08BZ, .15CT-.00BZ, .03CT-.18BZ, .09CT-.14BZ, .21CT-.06BZ, .27CT-.02BZ.

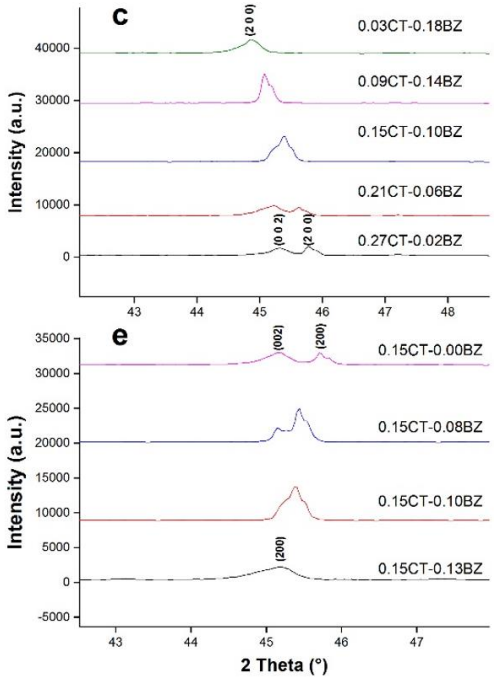

Figure 18: Higher resolution XRD peaks using a higher quality XRD machine show the shift in phase from rhombohedral to tetragonal.

Using High Score Plus, the lattice parameters of each composition was calculated. These values were used to pick a substrate with a good lattice match for epitaxial film growth in order to minimize strain in the material.

Table 2: Lattice parameters of sintered BCZT targets calculated from XRD patterns show the change in dimensions with composition.

Composition	Lattice Parameter (Å)
.15CT-.00BZ	3.99
.15CT-.08BZ	3.99
.15CT-.10BZ	4.00
.15CT-.13BZ	4.01
.03CT-.18BZ	4.04

.09CT-.14BZ	4.02
.21CT-.06BZ	4.00
.27CT-.02BZ	4.01

Figure 19: Image of a sintered target

Once these small pucks had been created and analyzed, the same batches of powder was used to create larger targets suitable for use in pulsed laser deposition. The only difference in procedure between the pucks and targets is the size and quantity of material. However, Table 3 shows that the targets are generally less dense than the pucks. All sintered pucks and targets of the same composition were made from the same homogeneous starting powder, so the grain size and distribution is not the cause of this discrepancy. This difference was likely due to the fact that the larger target was not pressed with as much pressure because of equipment limitations. A lower pressure would mean that there is more space initially between the grains, so sintering would not be able to densify the material as much.

Table 3: Percent density of the targets of BCZT is less than that of the smaller pucks.

Composition	Percent Density
.15CT-.00BZ	93.2%
.15CT-.08BZ	92.1%
.15CT-.10BZ	91.9%
.15CT-.13BZ	80.1%
.03CT-.18BZ	71.5%
.09CT-.14BZ	71.3%
.21CT-.06BZ	89.5%
.27CT-.02BZ	92.6%

Based on the density and capacitance measurements, the two targets of composition .15CT-.08BZ and .27CT-.02BZ appeared the most promising. Of these two, the .27CT-.02BZ composition was chosen somewhat arbitrarily to be used to make the films.

In order to make a successful thin film, several parameters of the PLD formula were optimized. The requirements of the film were that it was approximately 100 nm thick with good crystal structure. Films were grown on both a silicon substrate and a $SrTiO_3$ substrate. $SrTiO_3$ has a lattice constant of 3.9 Å and silicon has a lattice constant of 5.4 Å. XRD patterns of growth on these two substrates is shown in Figure 20. The red curve is an XRD of the sintered target. The large lattice mismatch between silicon and BCZT explains the relative lack of peaks on the silicon substrate. However, since the STO and BCZT lattices are only mismatched by about .1 Å, the {100}, {200}, and {300} peaks can be seen near the STO peaks showing epitaxial growth.

The bottom plot in Figure 21 shows an XRD pattern of and STO wafer without a film. By comparing to this plot, it can be seen that the BCTZ film adds a second peak to the STO peaks at 22 2θ, 46 2θ, and 73 2θ. Figure 21 shows the effect of cooling speed on crystal structure. It would be expected that cooling the film more slowly would give it time to form a more equilibrium phase at room temperature. However, there is very little difference between the XRD patterns of the slowly and quickly cooled samples. It is possible that the faster cooling speed tried in this experiment was slow enough for atoms to have time to rearrange.

Figure 22 shows the effect of increasing the partial pressure of oxygen during PLD. Lin, Wang, and Li found that increasing oxygen partial pressure decreases the lattice parameter of BCZT. [12] Figure 22 does indicate this. The BCZT peaks are shifter right, closer to the $SrTiO_3$ peaks at the higher PO_2.

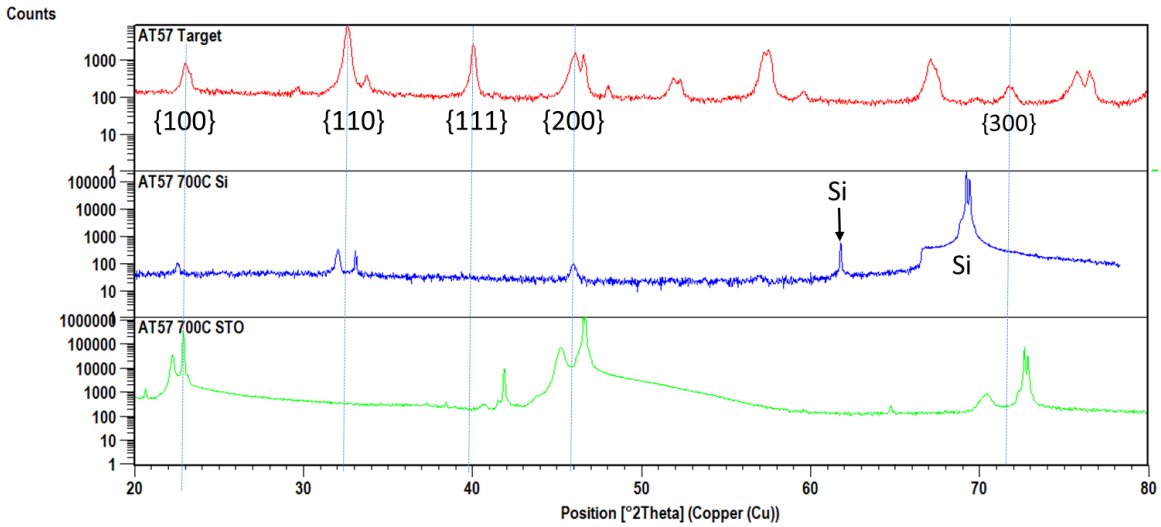

Figure 20: XRD of just the target of composition .27CT-.02BZ (top), of a ~100 nm film of .27CT-.02BZ BCZT on a silicon substrate (middle), and a ~100 nm film of .27CT-.02BZ BCZT on an STO substrate (bottom)

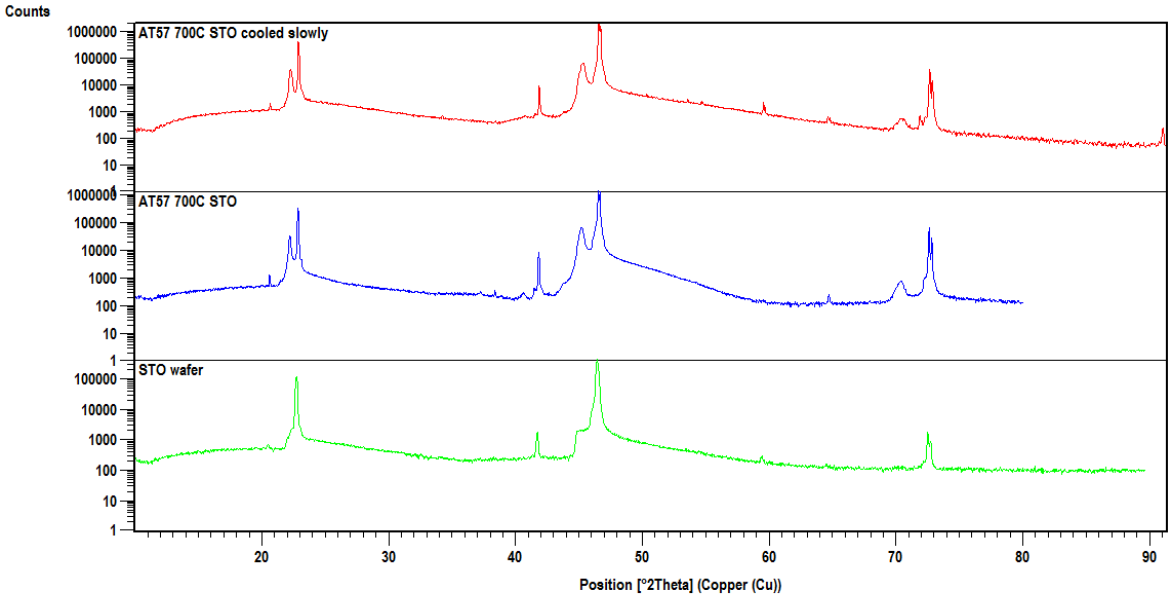

Figure 21: XRD pattern of .27CT-.02BZ film on STO slowed at 5 K/min (top) and 10 K/min (middle). Bottom is an XRD pattern of an STO wafer.

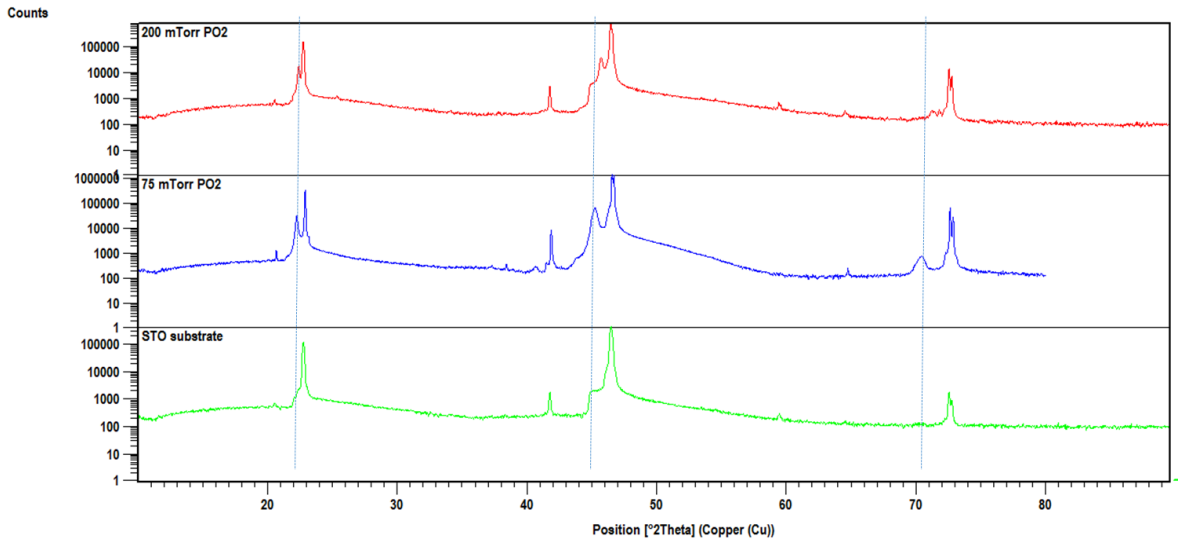

Figure 22: XRD showing the effect of partial pressure of oxygen during PLD on film structure.

Using the patterned contacts of the in-plane capacitor, capacitance was measured using the same low temperature capacitance setup as was used to measure the pucks, except two top contacts were used. Strontium titanate has a permittivity of around 400 F/m and the permittivity of the bulk BCZT is much higher, around 2500 F/m, so most of the electric field should be confined to the STO.

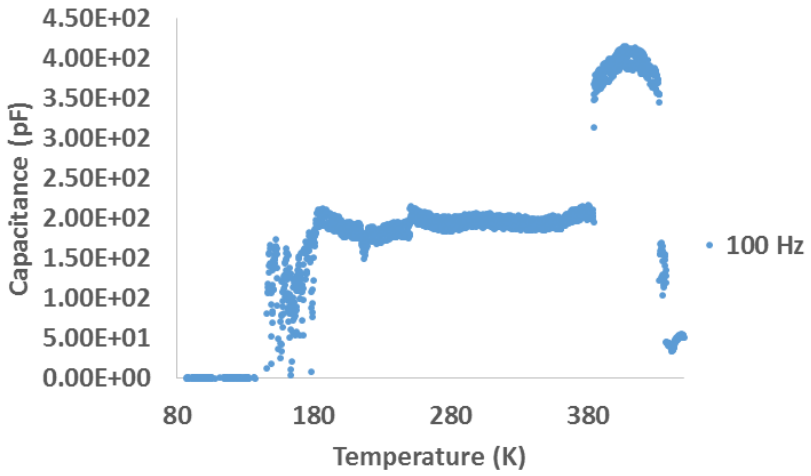

Figure 23: In-plane capacitance measurements from 87K-450K of thin film BCZT grown on STO.

Conclusion

A thin film BCZT material was fabricated and analyzed for use in a capacitive thermo-electric converter. Powdered sources of barium, calcium, titanium, and zirconium were ball milled in appropriate proportions to create several different compositions of BCZT around the triple point composition. These powders were then sintered and analyzed for density, dielectric properties, and crystallography

It was found that the most promising of the compositions tested were .15CT-.08BZ and .27CT-.02BZ. This was based on density measurements of the sintered material, XRD patterns showing the crystal structure, and capacitance measurements showing the change in capacitance over temperature. Capacitance measurements showed that the dielectric constant of BCZT does change significantly over temperature in the cubic phase and that the temperature range in which this occurs is approximately 380-440 K.

There are still several limitations to this capacitive thermo-electric converter. The operating temperature is about 100 K above room temperature which makes its applications somewhat limited. Future work on this topic would be to make a parallel plate capacitor to

measure the thin film capacitance more accurately and to study the heat transfer properties of thin film BCZT.

References

1. Olsen, R. B. Ferroelectric Conversion of Heat to Electrical Energy - A Demonstration. *J. Energy* **6,** 91–95 (1982).
2. Fang, J., Frederich, H. & Pilon, L. Harvesting nanoscale thermal radiation using pyroelectric materials. *J. Heat Transfer* **132,** 1–10 (2010).
3. Kozyrev, A. B., Platonov, R. A. & Soldatenkov, O. I. Thermal-to-electric energy conversion using ferroelectric film capacitors. *J. Appl. Phys.* **116,** (2014).
4. Wüstenhagen, V. The Promise and Problems of Thermoelectric Generators. *Adv. Nanotechnol.* **7,** 44–47 (2008).
5. Biswas, K. *et al.* High-performance bulk thermoelectrics with all-scale hierarchical architectures. *Nature* **489,** 414–8 (2012).
6. Clingman, W. H. & Moore, R. G. Application of ferroelectricity to energy conversion processes. *J. Appl. Phys.* **32,** 675–681 (1961).
7. Childress, J. D. Application of a Ferroelectric Material in an Energy Conversion Device. *J. Appl. Phys.* **33,** 1793–1798 (1962).
8. Volpyas, V. a., Kozyrev, a. B., Soldatenkov, O. I. & Tepina, E. R. Efficiency of thermoelectric conversion in ferroelectric film capacitive structures. *Tech. Phys.* **57,** 792–796 (2012).
9. Liu, W. & Ren, X. Large piezoelectric effect in Pb-free ceramics. *Phys. Rev. Lett.* **103,** 1–4 (2009).
10. Fang, B. J. *et al.* Preparation and electrical properties of pseudoternary $BaTiO_3$–$CaTiO_3$–$BaZrO_3$ lead free piezoelectric ceramics. *Adv. Appl. Ceram.* **112,** 257–262 (2013).
11. Petrov, P. Thin Film Deposition Lecture Notes. (2015).
12. Lin, Q., Wang, D. & Li, S. Strong Effect of Oxygen Partial Pressure on Electrical Properties of $0.5Ba(Zr_{0.2}Ti_{0.8})O_3$ -$0.5(Ba_{0.7}Ca_{0.3})TiO_3$ Thin Films. *J. Am. Ceram. Soc.* **98,** 2094–2098 (2015).

Appendix

Individual capacitance-temperature measurements of all eight compositions and their slopes.

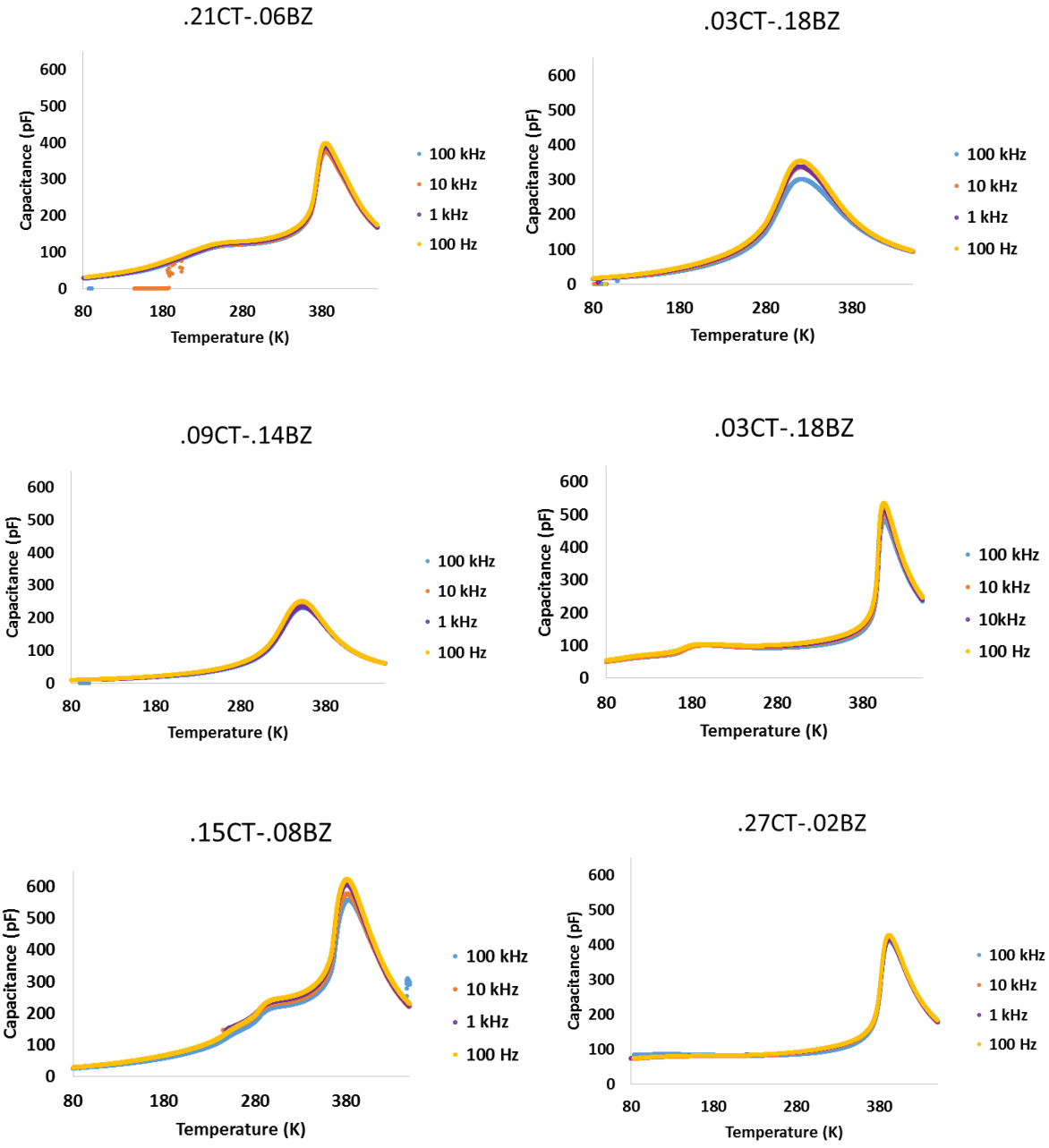

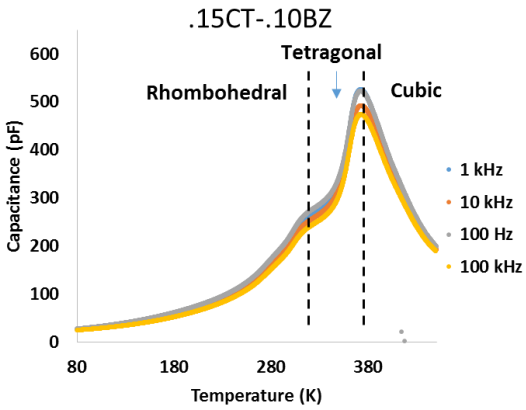
.15CT-.10BZ
Tetragonal
Rhombohedral
Cubic
Capacitance (pF)
600
500
400
300
200
100
0
80
180
280
380
Temperature (K)
1 kHz
10 kHz
100 Hz
100 kHz

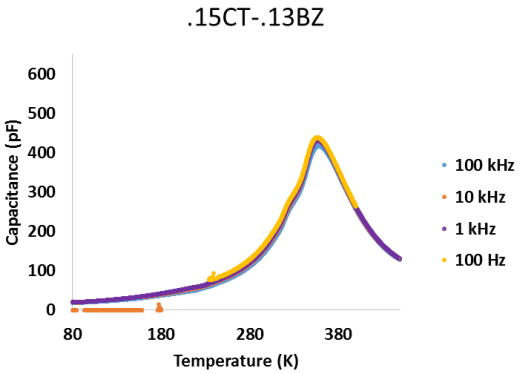
.15CT-.13BZ
Capacitance (pF)
600
500
400
300
200
100
0
80
180
280
380
Temperature (K)
100 kHz
10 kHz
1 kHz
100 Hz

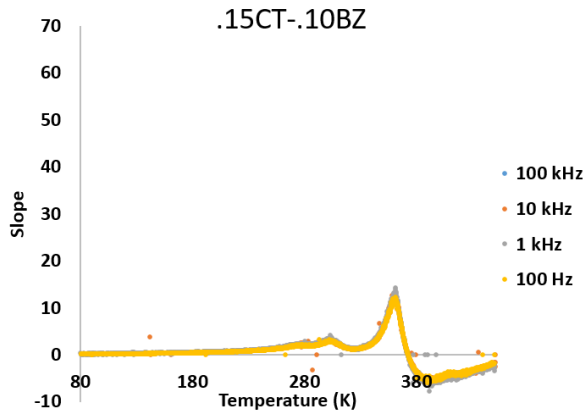
.15CT-.10BZ
Slope
Temperature (K)
100 kHz
10 kHz
1 kHz
100 Hz

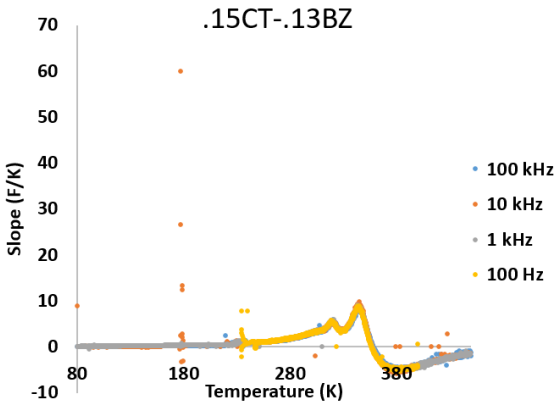
.15CT-.13BZ
Slope (F/K)
Temperature (K)
100 kHz
10 kHz
1 kHz
100 Hz

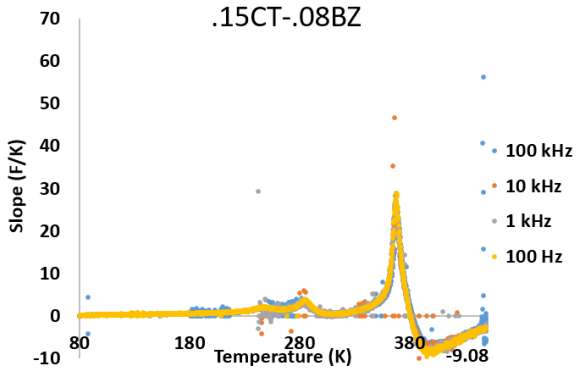
.15CT-.08BZ
Slope (F/K)
Temperature (K)
-9.08
100 kHz
10 kHz
1 kHz
100 Hz

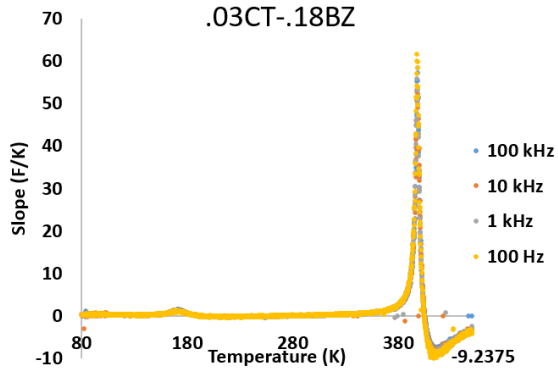
.03CT-.18BZ
Slope (F/K)
Temperature (K)
-9.2375
100 kHz
10 kHz
1 kHz
100 Hz

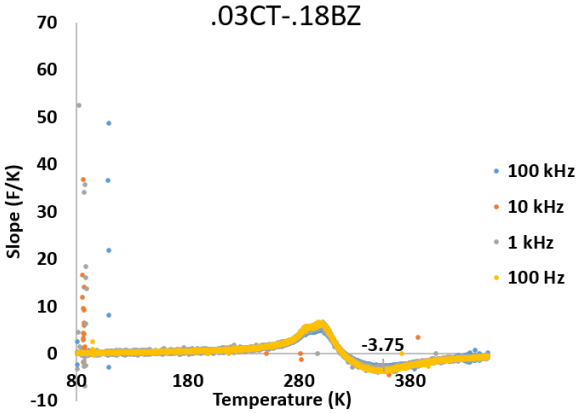
.03CT-.18BZ
Slope (F/K)
Temperature (K)
-3.75
100 kHz
10 kHz
1 kHz
100 Hz

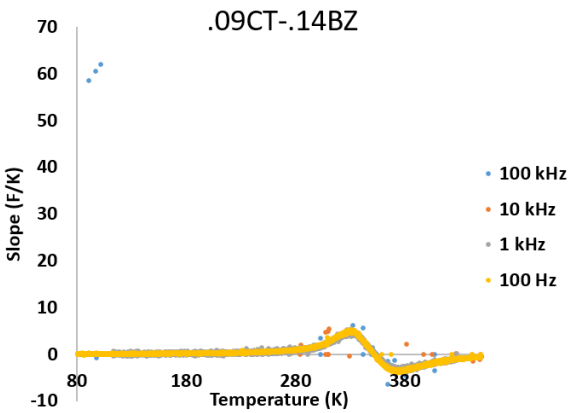
.09CT-.14BZ
Slope (F/K)
Temperature (K)
100 kHz
10 kHz
1 kHz
100 Hz

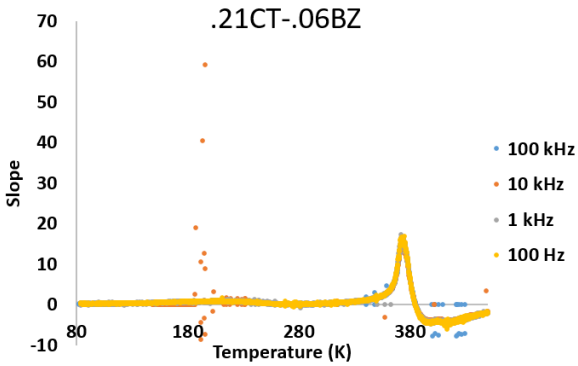
.21CT-.06BZ
Slope
Temperature (K)
100 kHz
10 kHz
1 kHz
100 Hz

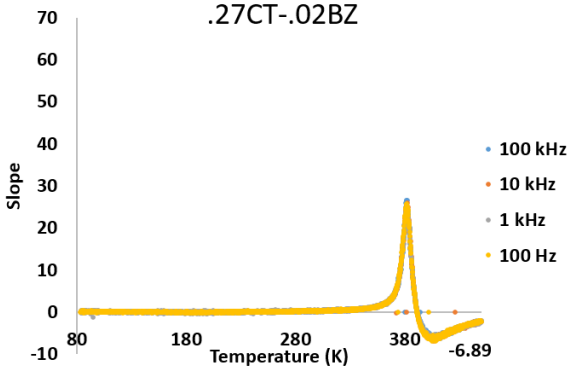
.27CT-.02BZ
Slope
Temperature (K)
-6.89
100 kHz
10 kHz
1 kHz
100 Hz